Investigations of Fatigue and Fracture Behavior of AA 7085

Rathin Maity, Akhilendra Singh, and Surajit Kumar Paul

The paper studies fatigue and fracture behavior of aluminum alloy AA 7085. Fatigue crack growth, low cycle fatigue (LCF), and High cycle fatigue tests have been performed at room temperature. Material's performance against the crack growth has been evaluated at load ratio of 0.1 and 0.3, parameters that govern crack growth are calculated using Paris and Walker model. XFEM has been used for the simulation of fatigue crack growth. Heaviside function is used for the modeling of crack surface while crack front is modeled by branch enrichment function. The simulation result presents a good match with experimental results. In LCF, cyclic softening was observed at higher strain amplitude. Fractographic features of the fracture surfaces obtained from the tests are examined by scanning electron microscopy.

1. Introduction

Aluminum alloys of seventh-generation (i.e., 7xxx series) are extensively employed in aerospace structures for their higher strength to weight ratio and heat treatability. There is an increased necessity for lightweight high strength aluminum alloy in existence for thicker plates. This enables the aerospace material's demand for integrated (joining free) structural components with a lesser number of parts to reduce the overall production cost (Ref 1, 2) of the component. Apart from reducing the manufacturing cost, the integrated aerospace structural component free from weld and riveted joints, increases overall life and reliability (Ref 3). But many of the contemporary seventh-generation aluminum alloys are produced in thin form as the thickness of the production of these alloys are restricted by their high quench sensitivity. So the demand for manufacturability in thick form without any compromise in any damage-tolerant properties has lead aerospace alloy developers to innovate new alloys for more reliability and reduced production cost. AA7085 is a new member of this series of alloys developed by Alcoa (Ref 4). Compared to AA 7075, it has lesser quench sensitivity, which allows producing components of thicker cross section (Ref 4, 5).

Due to the alloy's favorable properties, it has already found application in the massive bulkhead and wing spar structure of Airbus A380 (Ref 6). Despite its immense potential to replace currently used AA 707X and AA 705X series aluminum alloys (Ref 5, 7), the studies related to fatigue and fracture behavior of this alloy are hardly available in the literature. Dai et al. (Ref 8)

studied the high cycle fatigue behavior and crack propagation mechanism in the alloy. Luong et al. (Ref 9) studied the effect of laser peening and anodization processes on high cycle fatigue performance of the alloy. The relation between the fracture toughness of the material with its internal structure was

Rathin Maity, Akhilendra Singh, and **Surajit Kumar Paul**, Department of Mechanical Engineering, Indian Institute of Technology Patna, Bihta 801106, India. Contact e-mail: akhil@iitp.ac.in.

List of Symbols	
σ	Stress
ε	Strain
P_{min}	Minimum load in a cycle
P_{max}	Maximum load in a cycle
σ_{min}	Minimum stress in a cycle
σ_{max}	Maximum stress in a cycle
R	Load ratio Stress ratio
f	Frequency
K	Stress intensity factor
ΔK	Stress intensity factor range
ΔP	Force range
W	Width of Compact Tension (CT) specimen
B	Thickness of compact tension specimen
a	Crack length of compact tension specimen
K_{max}	Maximum stress intensity factor in a cycle
K_{min}	Minimum stress intensity factor in a cycle
k	Strength coefficient
n	Strain hardening exponent
σ_a	Stress amplitude in a cycle
σ_f'	Fatigue strength coefficient
N_f	Number of cycles to failure
b	Fatigue strength exponent
$\frac{\Delta \varepsilon_p}{2}$	Plastic strain amplitude
ε_f'	Fatigue ductility coefficient
c	Fatigue ductility exponent
H	Hardening factor
$\frac{da}{dN}$	Fatigue crack growth rate
C	Paris coefficient
m	Paris exponent
K_{mean}	Mean stress intensity factor
C_w γ_w and m_w	Walker material parameters

investigated by Shuey et al. (Ref 10). Burns et al. (Ref 11) studied the role of thickness on the alloy's environmental fatigue crack growth rate. Karabin et al. developed the constitutive model of the alloy (Ref 12).

Aerospace materials are exposed to demanding service conditions, thus there is a need for an extensive study of fatigue and fracture performance of AA7085. The use of damage tolerance approach in the aerospace industry requires the crack growth resistant properties in cyclic loading, the present study focuses on determining the fatigue crack growth (FCG), low cycle fatigue (LCF) and high cycle fatigue (HCF) performance of the materials. Two important fatigue crack growth rate models i.e., Paris and Walker model have been used to find the crack growth rate parameters in the stable crack growth zone. XFEM has been used to simulate the fatigue crack growth behavior of the material based on Paris model. Simulation results showed good match with experimental results.

2. Experimental Methodology

The thick rolled plate of AA7085 in T7X temper condition was purchased from the market. The composition of the alloy is shown Table 1. Flat type specimens were prepared using wire-cut electro discharge machining. All the tests were conducted in room temperature using a servo-hydraulic test system of 100 kN capacity. The parameters of the tests (like waveform, frequency, load range, load ratio for fatigue crack growth rate test) were fed to the system via a software running on a computer which was interfaced to the controller of the test system.

The tensile test was performed according to ASTM E8M with a strain rate of 6.67×10^{-4}/s. Specimens of 25 mm gauge length and 4 mm thickness were selected for tensile test.

The HCF test was conducted following the ASTM E466-15 standard. Axial load of constant amplitude was applied on a well-polished flat specimen of 8mm width (at minimum cross-sectional area) and 4mm thickness at a load ratio of -1 (Eq 1) and 30 Hz frequency. The waveform of the loading cycle was chosen as sinusoidal.

$$R = \frac{P_{\min}}{P_{\max}} = -1 \tag{Eq 1}$$

The testing procedure of the LCF test was followed as per ASTM E606. Flat specimens of 15 mm gauge length, 10 mm width and 5 mm thickness were selected for the tests. The mirror surface finish of the specimen was ensured by polishing it gradually from emery paper of lower grade (larger particle size) to diamond paste of particle size 0.25 μm. A strain control channel was used for the test, with triangular waveform and mean strain equals to zero. The tests were in performed in four different strain amplitudes of 0.6, 0.7, 1, and 1.5%. The strain

rate was kept to 10^{-3}/s which is related to the frequency of the test by following relation (Ref 13).

$$f = \frac{\mathrm{d}\varepsilon/\mathrm{d}t}{4\left(\frac{\Delta\varepsilon}{2}\right)} \tag{Eq 2}$$

An extensometer of gauge length 12.5 mm was mounted on the specimen for the control of strain. For the purpose of analysis, 200 data points per cycle were collected.

ASTM E647-15 was the guideline for the fatigue crack growth rate test. Out of several types of specimens recommended by ASTM, compact tension (CT) specimens of 50mm width and 12.5 mm thickness were selected as the shape this type of specimen reduces the wastage of material during machining. To reduce the effect of notch radius, a pre-crack was generated as per ASTM instruction. The pre-cracking was done ensuring that the final $K_{\max}$ at the end of pre-cracking does not surpass the initial $K_{\max}$ of the main test. To fulfill this criterion decreasing stress intensity factor range (ΔK) procedure is adopted for the pre-cracking. In this method, the test control system reduces the force range (ΔP) gradually, in order to decrease the stress intensity factor range as the crack length increases. The normalized rate of stress intensity factor range change is called the crack gradient given by the expression $\frac{1}{\Delta K}\frac{\mathrm{d}\Delta K}{\mathrm{d}a}$. The value of the normalized crack gradient was taken as -0.03. During the ΔK decreasing test, at any crack length, the necessary force range ΔP is computed by the test system by the following relation

$$\Delta K = \frac{\Delta P}{B\sqrt{W}}\frac{(2+\alpha)}{(1-\alpha)^{3/2}}\left(0.886 + 4.64\alpha - 13.32\alpha^2 + 14.72\alpha^3 - 5.64\alpha^4\right) \tag{Eq 3}$$

where $\alpha = \frac{a}{W}$.

After completion of pre cracking the initial maximum stress intensity factor $K_{\max}$ is selected in such a manner that it is greater than the final maximum stress intensity factor of the pre cracking test. For a given load ratio R, the initial stress intensity factor range of the main test is calculated by the following relation

$$\Delta K = (1 - R)K_{\max} \tag{Eq 4}$$

As we proceed to perform the test by constant force amplitude method the necessary force range (ΔP) is calculated by Eq 3.

3. Fatigue Crack Growth Model of Paris and Walker

According to Paris law (Ref 14, 15), the subcritical crack growth rate in fatigue follows a power-law relationship with stress intensity factor range above the threshold zone of crack growth, shown in Eq 5.

Table 1. Composition of the alloy (wt.%)

Elements	Al %	Zn %	Mg %	Cu %	Fe %	Si %	Zr %
	89.323	7.215	1.792	1.452	0.067	0.056	0.029
Reference (Ref 5)		7-8	1.2-1.8	1.3-2.0	0.08	0.06	0.08

$$\frac{\mathrm{d}a}{\mathrm{d}N} = C(\Delta K)^m \tag{Eq 5}$$

The stress intensity factor range (ΔK) is related to maximum stress intensity factor and minimum stress intensity factor, respectively, by Eq 4 and Eq 6.

$$K_{\min} = \Delta K \frac{R}{(1-R)} \tag{Eq 6}$$

The mean stress intensity factor can be calculated from Eq 4 and Eq 6.

$$K_{mean} = \frac{K_{\max} + K_{\min}}{2} = \frac{\Delta K}{2}\left(\frac{1+R}{1-R}\right) \tag{Eq 7}$$

The Paris model's limitation is that it does not predict fatigue crack growth rate for different load ratios because of the Paris constant C changes with load ratio. To use the damage tolerance approach effectively parameters of fatigue crack growth model incorporating the effect of load ratio is essential. Walker proposed a new model that takes account of the effect of load ratio in the crack growth rate equation (Ref 16, 17). The following relationship expresses Walker model.

$$\frac{\mathrm{d}a}{\mathrm{d}N} = C_w \left[\frac{\Delta K}{(1-R)^{1-\gamma_w}}\right]^{m_w} \tag{Eq 8}$$

where C_w, γ_w and m_w are material parameters.

The Walker model can be rewritten as

$$\frac{\mathrm{d}a}{\mathrm{d}N} = \left[\frac{C_w}{(1-R)^{m_w(1-\gamma_w)}}\right](\Delta K)^{m_w} \tag{Eq 9}$$

This indicates that the Paris constant C is replaced with an explicit function of load ratio R (Eq 10) and the constant γ_w which signifies the degree of dependency of fatigue crack growth rate on load ratio (Ref 18).

$$C = \frac{C_w}{(1-R)^{m_w(1-\gamma_w)}} \tag{Eq 10}$$

And the Paris exponent (m) is the same as Walker exponent (m_w) (Ref 19).

4. Review of Extended Finite Element Method (XFEM)

The fatigue crack growth of material has been simulated using extended finite element method. A generalized APDL (ANSYS) code is written using XFEM methodology. The extended finite element method incorporates crack-like discontinuities in the displacement function, which removes the necessity of modeling the crack geometry in the domain explicitly. The main advantage of XFEM is that for each step of crack growth remeshing is not needed, which reduces the computational difficulty. The main drawback of modeling the crack growth problem in FEM is conformal meshing which is well taken care of by XFEM. A typical XFEM domain with discretization is shown in Fig. 1. The enriched displacement function in XFEM is written as (Ref 20)

$$\mathbf{u}^h(\mathbf{x}) = \sum_i \varphi_i(\mathbf{x})\mathbf{u}_i + \sum_{j \in P} \varphi_j(\mathbf{x})H(\mathbf{x})\mathbf{a}_j + \sum_{k \in Q} \varphi_k(\mathbf{x})\left(\sum_{\gamma=1}^4 F_\gamma(\mathbf{x})\mathbf{b}_k^\gamma\right) \tag{Eq 11}$$

where $\varphi_i(\mathbf{x})$ is Lagrange nodal shape function; $\mathbf{u}_i$ is nodal displacement vector. The discontinuity of displacement between two sides of crack is taken care of by Heaviside step function which takes on value of +1 and -1 depending on the location of the sampling point and $\mathbf{a}_j$ in the expression indicates additional enriched nodal degrees of freedom which takes account of jump in displacement. $F_\gamma(\mathbf{x})$ is the crack tip enrichment function (branch function), used to capture high-stress gradient near the crack tip and $\mathbf{b}_k^\gamma$ is the additional nodal degrees of freedom in the crack tip singularity zone.

The branch functions which are used in the singularity zone at the crack tip for enrichment are (Ref 20)

$$F_\gamma(\mathbf{x}) = \left[\sqrt{r}\cos\frac{\psi}{2}, \sqrt{r}\sin\frac{\psi}{2}, \sqrt{r}\sin\frac{\psi}{2}\sin\psi, \sqrt{r}\cos\frac{\psi}{2}\sin\psi\right] \tag{Eq 12}$$

5. Results and Discussion

5.1 Microstructural Results

The sample of the as-received AA7085 alloy was polished up to 0.25 μm size of diamond paste. Then it was etched by modified Poulton's reagent whose composition was 21.25 mL water, 20 mL Nitric acid, 15 mL Hydrochloric acid, 6gm Chromic acid, 1.25 mL Hydrofluoric acid. The etched surface was observed under a field emission scanning electron microscope for micrograph which is shown in Fig. 2(a). From the micrograph, it is visible that the grains are elongated in the rolling direction with clear boundaries. The average grain size is $5.4\mu m$, calculated by the average line intercept method. Some particles of intermetallic phase of Al_2CuMg are also seen in the results in Fig. 2(a).

5.2 Tensile Test

The engineering stress-strain plot of the as-received alloy is shown in Fig.2b. The conventional mechanical properties are determined from the monotonic tensile test (Table 2). The Hollomon parameters (Eq 13), strength coefficient (k) and strain hardening exponent (n) are evaluated as 620 (MPa) and 0.0467, respectively.

$$\sigma = k\varepsilon^n \tag{Eq 13}$$

Scanning electron microscopic fractography of fractured tensile sample is shown in Fig. 3. Dimples with second phase inclusion particle of Al_2CuMg inside it (Ref 21), is seen from the fractography. This indicates the ductile nature of the fracture mechanism where a microvoid is nucleated by formation of a free surface either by cracking or by decohesion of the phase interface followed by growth of the microvoids and coalescence of the microvoids with the vicinal microvoids (Ref 22). After certain growth of the voids, final fracture occurs keeping the dimples as the reminiscence of microvoid formation
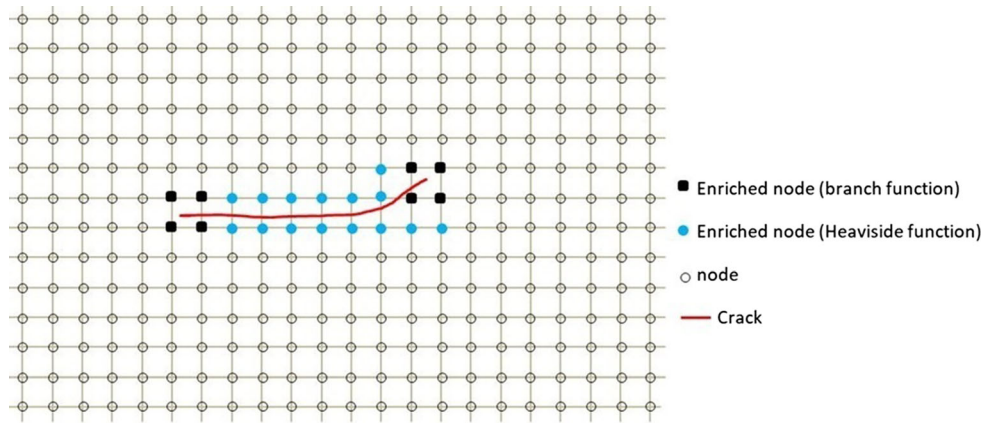
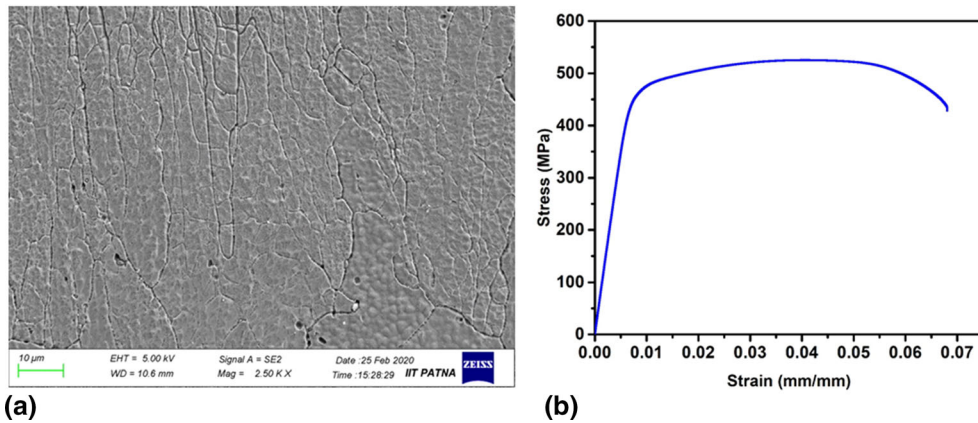**Fig. 1** Schematic diagram of a typical crack geometry in XFEM domain

(a) **(b)**

Fig. 2 (a) Microstructural image of as received AA7085 (b) Engineering stress strain plot of AA 7085

Table 2. Mechanical properties of the alloy

Property	Value
Yield Stress	463 MPa
Ultimate tensile strength	525 MPa
Young's modulus	69 GPa
Percentage of elongation	6.8

fracture mechanism. Though the microscopic nature of the fracture surface shows ductile fracture mechanism, macroscopically necking is not seen during the test.

5.3 High Cycle Fatigue Test

The stress amplitude versus the number of cycles to failure for stress ratio equals to −1 is shown in Fig. 4. Basquine equation (Eq 14) is used to fit the stress amplitude (σ_a) and the corresponding number of cycles to failure (N_f).
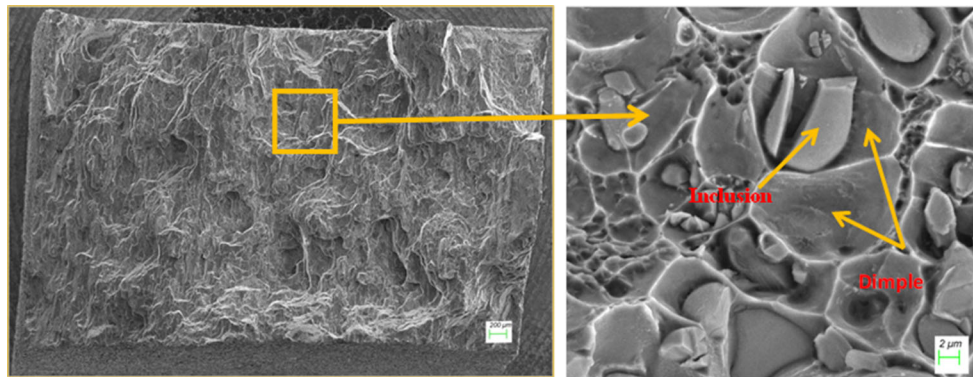
Fig. 3 Fracture surface morphology during tensile test of AA7085

$$\sigma_a = \sigma_f'(2N_f)^b \qquad \text{(Eq 14)}$$

The Basquine constants σ_f' and b have been calculated, upon substituting which the equation takes the form as follows

$$\sigma_a = 5248(2N_f)^{-0.2885} \qquad \text{(Eq 15)}$$

From Eq15 the endurance strength of the alloy calculated based on 10^6 cycles is 79.8 MPa.

A field emission scanning electron microscope examined the fracture surface of the specimens is presented in Fig. 5. From the fatigue fracture zone, the striation marks (indicated by arrows) which characterize the crack front mark in stable crack propagation zone in fatigue, are seen from fig. Dimple sizes of two different orders are observed from the fast fracture zone due to the two different distributions of secondary phase inclusion particle distributions. The contribution of submicron level trans granular precipitates in void formation is evident from some very fine size dimples from fig. The fracture mechanism in high cycle fatigue for this alloy has been extensively studied by Dai et al (Ref 8). Their study reveals that major dimples in the fast fracture zone, nucleate from the Fe rich particles.

5.4 Low Cycle Fatigue Test

The results of plastic strain amplitude vs. number of cycles to failure are illustrated in Fig. 6 on a double logarithmic scale. The linear relationship in double logarithmic scale indicates the existence of a power-law type relation (Coffin Manson equation) between plastic strain amplitude and life in terms of number of cycles to failure.

$$\frac{\varepsilon_p}{2} = \varepsilon_f'(2N_f)^c \qquad \text{(Eq 16)}$$

Substituting the values fatigue ductility coefficient (ε_f') and fatigue ductility exponent (c) the equation takes the following form
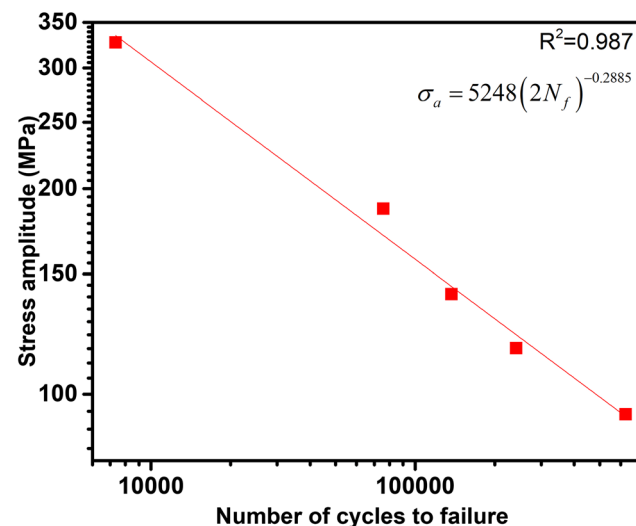

Fig. 4 S N diagram of the AA7085

$$\frac{\varepsilon_p}{2} = 4.9(2N_f)^{-1.3} \qquad \text{(Eq 17)}$$

Figure 7 depicts the stress response of the alloy for different strain amplitudes. Cyclic softening was observed except the lowest strain amplitude. The material's cyclic stress response is similar to AA 7075 (Ref 23). The cyclic softening behavior of the material in the present investigations is following the thumb rule in cyclic plasticity that soft material hardens and hard material softens (Ref 24) because inelastic strain cycling in hard materials rearranges the dislocation arrangement such a way that the resistance to deformation decreases resulting softening in the material (Ref 18). The plot of strain ratio (plastic strain amplitude to elastic strain amplitude) with the number of cycles is illustrated in Fig. 8(a).

A concise and unified approach of quantifying cyclic hardening and softening introduced by Paul et al. (Ref 25) has been used in this study. In this approach, the hardening factor is defined as

$$H = \text{ strain ratio in any cycle/strain ratio in the first cycle} \qquad \text{(Eq 18)}$$

The equation indicates that $H < 1$ for cyclic hardening and $H > 1$ for cyclic softening. Fig. 8(b) illustrates the hardening factor for different strain amplitudes.

The hysteresis loop of different strain amplitudes are shown in Fig. 9(a). Cycle corresponding to half-life was considered for the hysteresis plot. The area enclosed by the hysteresis loop increases with the increment strain amplitude of the test indicating that the energy dissipation increases for an increment in strain amplitude. The dissipated energy causes irreversible damage in the material like crystal slip and heat generation (Ref 26). The non-Masing behavior of the alloy is displayed in Fig. 9(b). The tips of hysteresis loops were shifted to the common origin to check whether the loading curve matches or not.

The combined elastic and plastic strain life plot combining HCF and LCF results are presented in Fig. 10. It is observed that for low cycle fatigue cases, both elastic and plastic strain contribute to the total strain and the number of cycles to failure has a strong correlation with plastic strain amplitude. The plastic strain is responsible for nucleation of embryo crack by the formation of extrusion and intrusion on the surface of the material, which leads to failure of the material after a certain number of cycles (Ref 18). Multiple crack initiation sites were observed from the scanning electron microscopy of a failed LCF specimen's surface as shown in (Fig. 11). From these results, it is observed that the cracks originated from the lateral surface, which is perpendicular to the loading axis of the specimen. For high cycle fatigue cases, the plastic strain is absent in the continuum level, only elastic strain contributes to the total strain. In this case, the micro-irregularities like microstructural inhomogeneity and very small scale surface asperity and on the surface act as local stress raisers, creating local micro plasticity that nucleates a crack (Ref 27). A decrease in gross elastic strain amplitude in the continuum level decreases the severity of local plasticity, which increases the life of the material, obvious from Fig. 10.
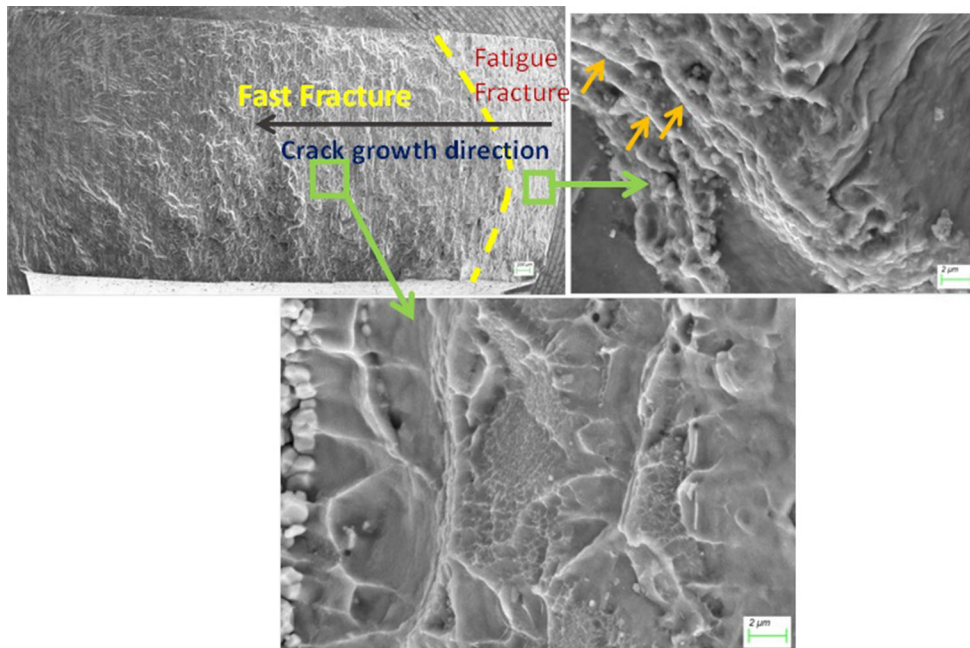
Fig. 5 Fracture surface morphology during high cycle fatigue test of AA7085. (Striation marks indicated in the fatigue fracture zone by arrow marks)
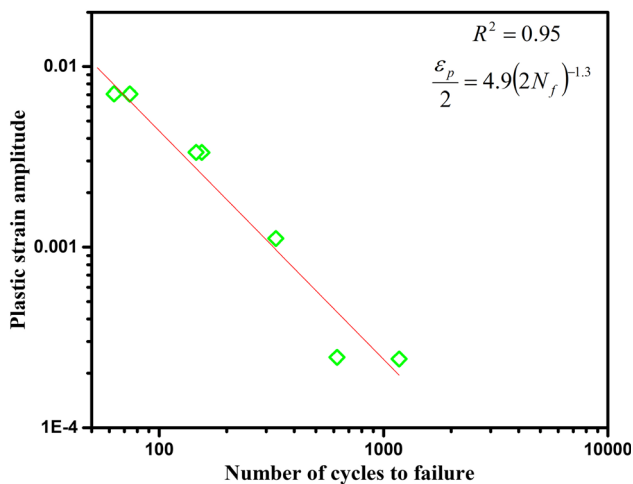

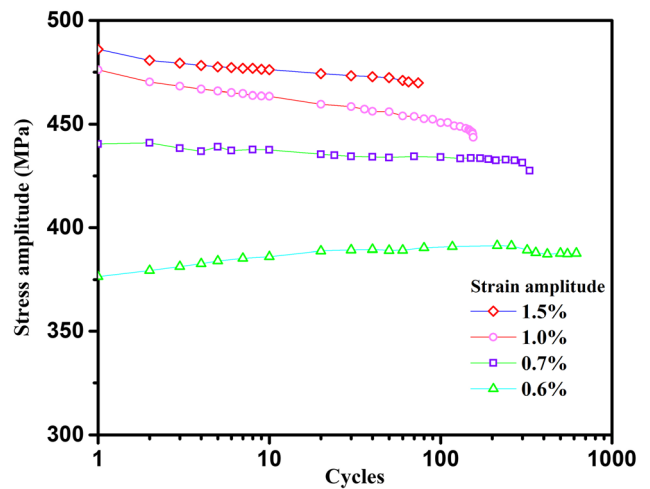**Fig. 6** Plastic strain amplitude vs. number of cycles to failure

Fig. 7 Cyclic stress response of investigated AA7085

5.5 Fatigue Crack Growth Rate Test

The fatigue crack growth rate tests were performed on two different load ratios $R = 0.1$ and 0.3. Paris constants C and m calculated by curve fitting are shown in Table 3. The fatigue crack growth rate vs. stress intensity factor range plot is shown in Fig. 12. Due to their power-law type relationship, the plot is linear in the logarithmic plot. At any ΔK, the fatigue crack growth rate for load ratio 0.3 is seen higher than that of load ratio 0.1 due to the fact that the mean stress intensity factor increases with the increment of load ratio, which can be understood from Eq7.This effect of mean stress intensity factor is responsible for shifting the curve to up and left, which increases the value of Paris constant C due to increment of y intersection. A similar shift in stable crack growth zone has been reported for other alloys of this series like AA7075 (Ref 28, 29).

For a particular load ratio and constant load range controlled test, the stress intensity factor range is seen to increase from the x-axis of the plot, as the crack growth due to fatigue increases the stress intensity factor which is evident from Eq 3. This gradual increment in stress intensity factor range (ΔK) increases the maximum stress intensity factor (K_{max}) gradually in the specimen related to the relation shown in Eq4. When this maximum stress intensity factor achieves the brittle fracture toughness of the material, sudden crack propagation is seen (Ref 30). For the higher load ratio, fatigue crack growth rate is observed from a comparatively lower stress intensity factor range than that of lower load ratio due to decrement of threshold stress intensity factor range ΔK_{th}.

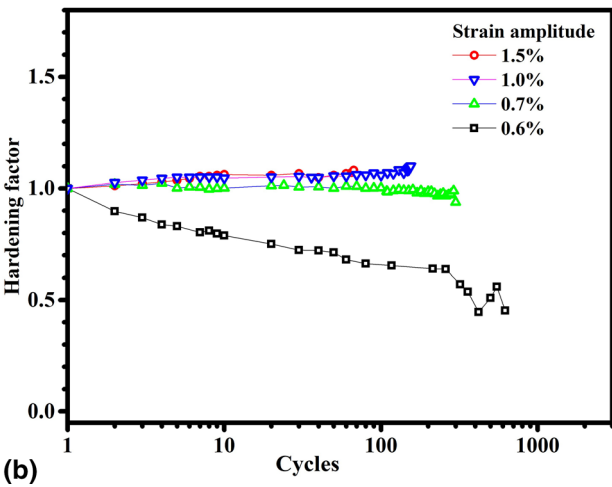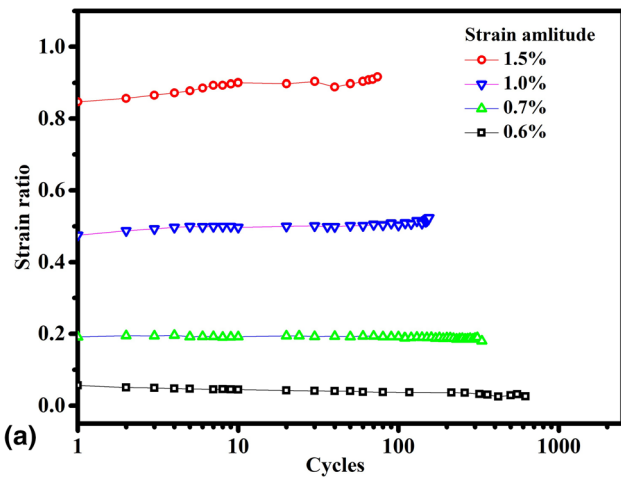The Paris exponent is supposed to be independent of load ratio R. For the load ratio 0.1 and 0.3 the exponent varied

Fig. 8 (a) Strain ratio vs. number of cycles (b) Variation of hardening factor with number of cycles at different strain amplitude

Fig. 9 (a) Stabilized hysteresis loop of AA7085 at different strain (b) Analysis of Masing behavior: Stable hysteresis loops with matched compressive tips at the origin

around 4%, so their arithmetic mean is considered for calculation of Walker parameters i.e., $m_w = 3.745$

Substituting the values of Paris constant for the two load ratio (i.e., load ratio) in Eq 10, the following equations are obtained

$$3.8 \times 10^{-8} = \frac{C_w}{(1 - 0.1)^{3.745(1 - \gamma_w)}} \qquad \text{(Eq 19)}$$

$$6.6 \times 10^{-8} = \frac{C_w}{(1 - 0.3)^{3.745(1 - \gamma_w)}} \qquad \text{(Eq 20)}$$

Solving Eq 19 and Eq 20 the Walker parameters are calculated as

$$C_w = 3.015 \times 10^{-8} \frac{\text{mm/cycle}}{(\text{MPa}\sqrt{\text{m}})^m}$$

and $\gamma_w = 0.4134$

For most of the metals the value of γ_w is around 0.5 (Ref 18, 19) which is closer to our result.

Substituting the values of material parameters in Eq 8, the Walker model for the material becomes
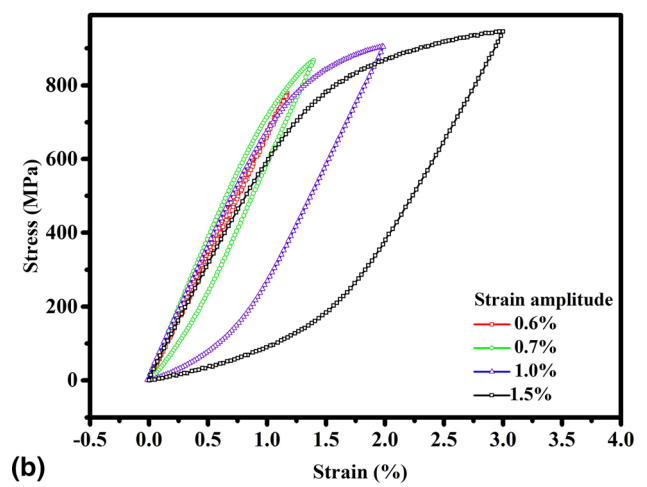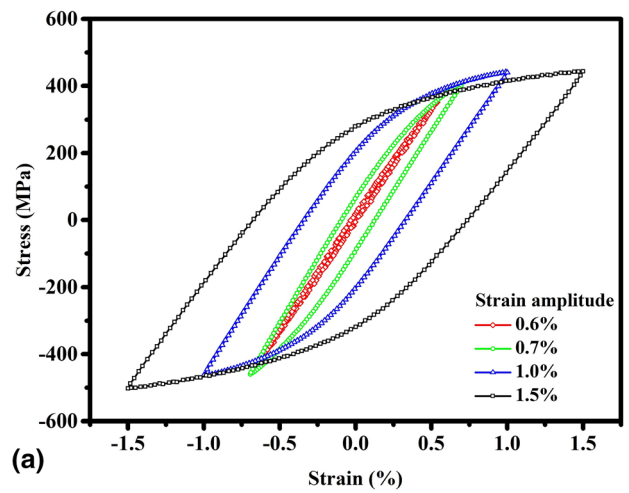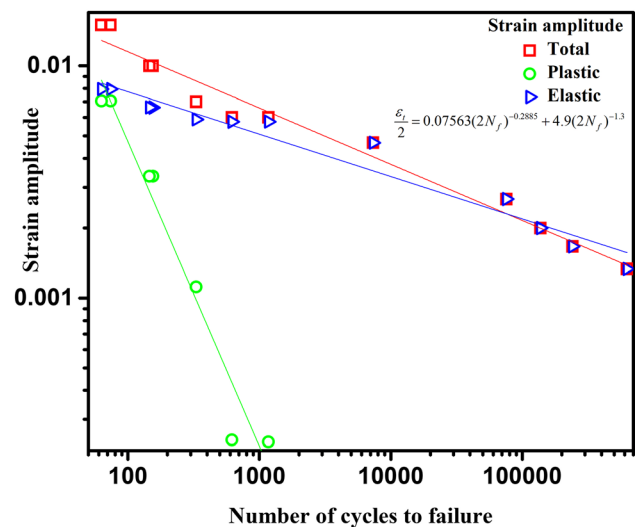

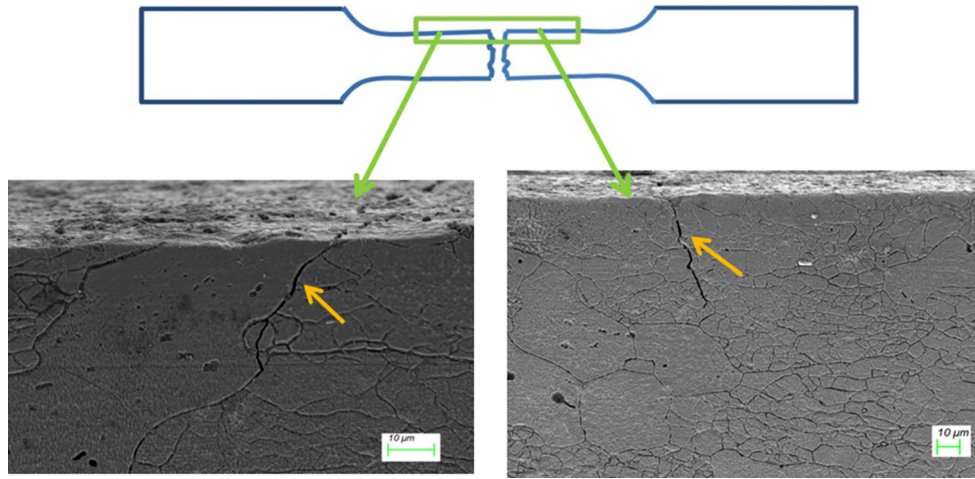Fig.10 Combined Basquine and Coffin-Manson plot of AA7085

Fig. 11 Multiple crack initiation sites in gage length portion in LCF test

Table 3. Paris constants C and m calculated by curve fitting

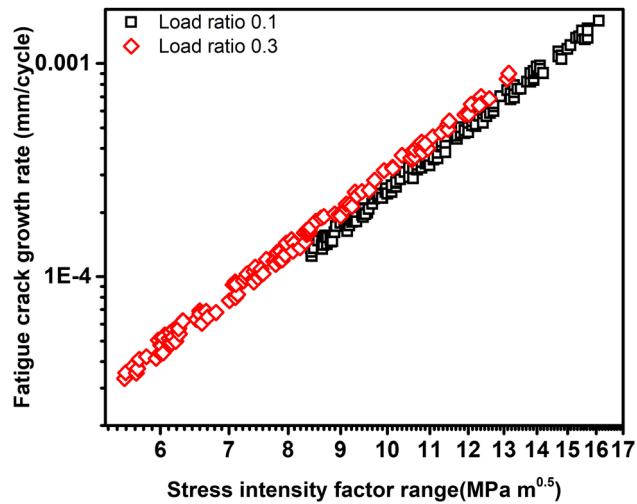| Stress ratio R	$C \left[\frac{mm/cycle}{(MPa\sqrt{m})^m} \right]$	m
0.1	3.80×10^{-8}	3.82
0.3	6.60×10^{-8}	3.67

Fig. 12 Fatigue crack growth of the alloy at load ratio 0.1 and 0.3

$$\frac{\mathrm{d}a}{\mathrm{d}N} = 3.015 \times 10^{-8} \left[\frac{\Delta K}{(1-R)^{0.5866}} \right]^{3.745} \tag{Eq 21}$$

The fatigue fracture zone and the zone of fast fracture can be seen from Fig. 13(a). Striation marks, characteristics of the fatigue fracture zone, are seen from Fig. 13(b). Some of the striation widths (shown in the figure by the double arrow) are larger than the fatigue crack growth rate (crack growth due to one cycle) for any stress intensity factor range shown in Fig. 12. This indicates that two consecutive striation marks are not always created two consecutive cycles, which is contrary to popular belief that there is always one to one relation between striation marks and loading cycles. This is also evident from the results shown in Fig. 13(c). It can be spotted from the lower portion of this figure, that the striation mark A and B indicate two consecutive loading cycle as there is no crack front mark between them but upon careful observation on the upper portion of the striation marks, it can be seen that there are few very small striation marks between the striation mark A and B. So there are clearly some loading cycles between cycles corresponding to striation mark A and B whose effect as a crack front mark is absent in the lower portion of the fig. Similar phenomena is observed from the enclosed zone (marked dotted) of Fig. 13(b) where the effect of two intermediate striation marks is absent. This indicates that there may be some cases where between two cycles corresponding to two consecutive striation marks there may be cycles whose effect on fracture surface as a crack front mark are completely absent, denoting
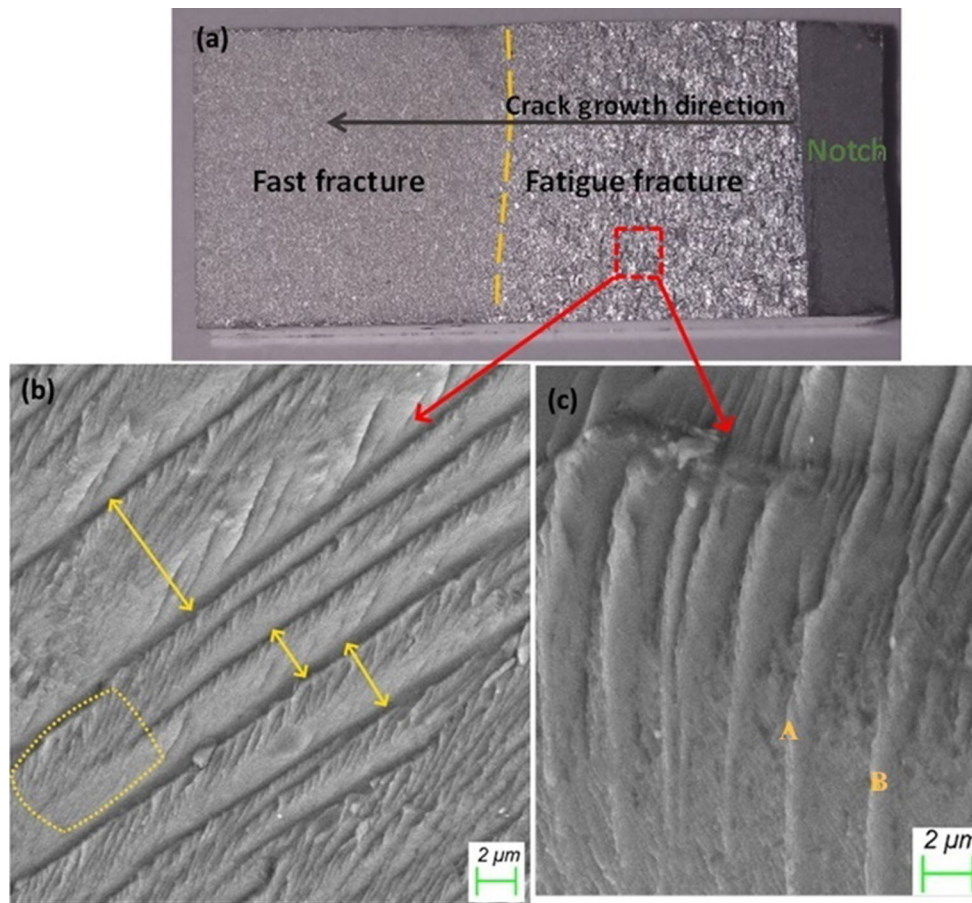
Fig. 13 (a) Fracture surface of CT specimen in Fatigue Crack Growth Rate test (b) Striation marks in fatigue fracture zone, (large striation width is shown in double arrow) (c) Intermediate striation marks between striation mark A and B (seen in above portion) whose effect is absent in lower portion of the figure

that every cycle does not contribute to crack front mark on the surface. This does not mean that these cycles do not contribute to the fatigue damage on the crack propagation mechanism. This is supported by studies that say in some cases striations form due to accumulated damage of several cycles (Ref 31).

6. Simulation of Fatigue Crack Growth Rate

A generalized APDL code has been written to simulate the crack growth by 2D XFEM for the two load ratios. The simulation is Paris law based so it is applicable for region two fatigue crack growth zone only. The simulation takes continuum material property, Paris constants, geometry, and loading conditions (i.e., load range and load ratio) as input and provides growth of the crack in the different number of cycles as output. The major assumptions in this simulation are that the material has to be linearly isotropic; Crack closure and plasticity effect near the crack tip is not considered. The fatigue crack growth is

modeled by either the life cycle method or cycle by cycle method depending on the nature of loading. The life cycle method has been used in this simulation which is used for constant amplitude cyclic loads. The solution procedure is static (because stress intensity factor range which is required for the prediction of crack growth can be determined static analysis method). The finite element program determines K_{max} at the maximum load P_{max} which is provided in the boundary conditions, and then it calculates ΔK using load ratio. Using already calculated ΔK and user-specified Δa, the program calculates ΔN for that sub-step by Paris law (shown in the difference form of Paris law in Eq 22).

$$\frac{\Delta a}{\Delta N} = C(\Delta K)^m \tag{Eq 22}$$

The crack length is updated and K_{max} is calculated for the subsequent step, the procedure continues until the desired number of sub-steps is completed. A two dimensional model of CT specimen is created. Maximum load (P_{max}) per unit thickness was applied to incorporate the thickness effect of the
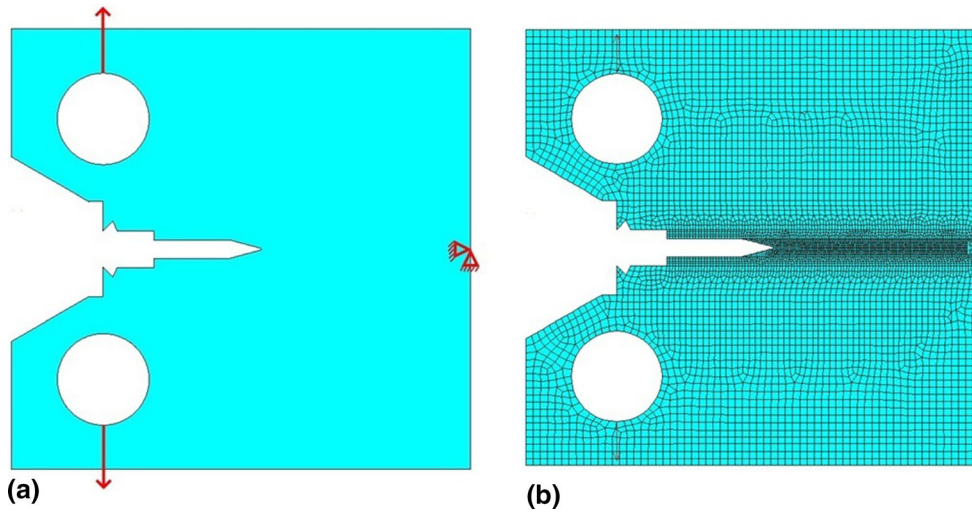
Fig. 14 (a) 2D solid model and (b) meshed model of CT specimen with boundary conditions
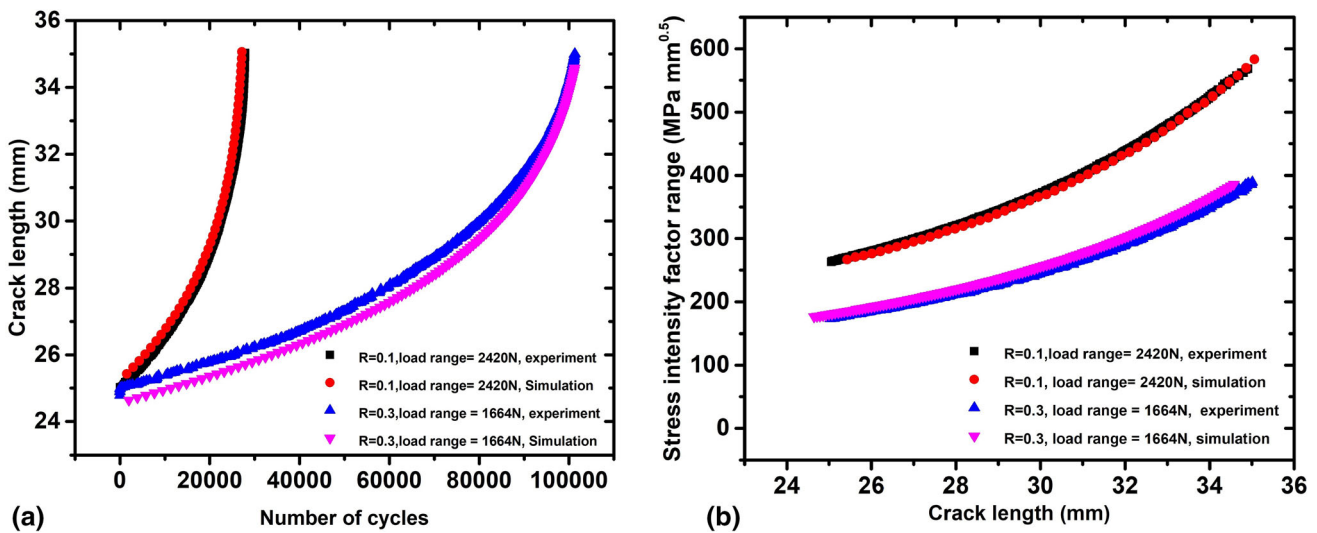

Fig. 15 Experimental and simulation results of (a) number of cycles vs. crack growth (b) Stress intensity factor range vs. crack length

specimen. Two-dimensional solid model and meshed model with boundary conditions is presented in Fig 14(a) and (b), respectively. A total of 23572 nodes (including the enrichment nodes) are created in the domain for the simulation at load ratio 0.1. For simulation at load ratio 0.3, total number of nodes was 177367. The crack growth (a) vs. number of cycles (N) plot is presented in Fig. 15(a). For load ratio 0.1 and load range ΔP 2420N, it is seen that the simulation result is very close to the experimental one in this case. For load ratio 0.3 and load range 1664N, it is observed that there is marginal difference between the experimental and simulation results in the initial cycles, however, this difference has converged at larger crack length which is evident from the plot. The slope between crack growth and number of cycles plot is seen steeper (for each loading cases) in larger crack length which indicates that the number of cycles required for unit length of crack growth is lesser in larger crack length. This is because the fatigue crack growth rate increases with increment in stress intensity factor range which is a monotonic increasing function of crack length. The

monotonic increasing relation of Stress intensity factor range (ΔK) with crack growth (a) plot is presented in Fig. 15(b). For a particular crack length, the stress intensity factor range for load range 2420N is higher than the load range 1664N because stress intensity factor is proportional to load range for particular crack length and given geometry which can be seen from Eq 3. The displacement field and equivalent stress contour at the end of the last sub-step for this loading condition is shown in Fig. 16. The displacement field is seen to be symmetric with respect to the crack growth direction and its magnitude increases with the distance from the un-cracked portion where the magnitude of displacement is very small. High stress gradient is observed at the crack tip. The maximum stress is seen at a very small area at the crack tip zone and its value shown in the fig is quite higher due to linear elastic assumption which is untrue for the crack tip plasticity zone. However, overall simulation results predict the fatigue crack growth well, as a very good match with the experimental results is observed.
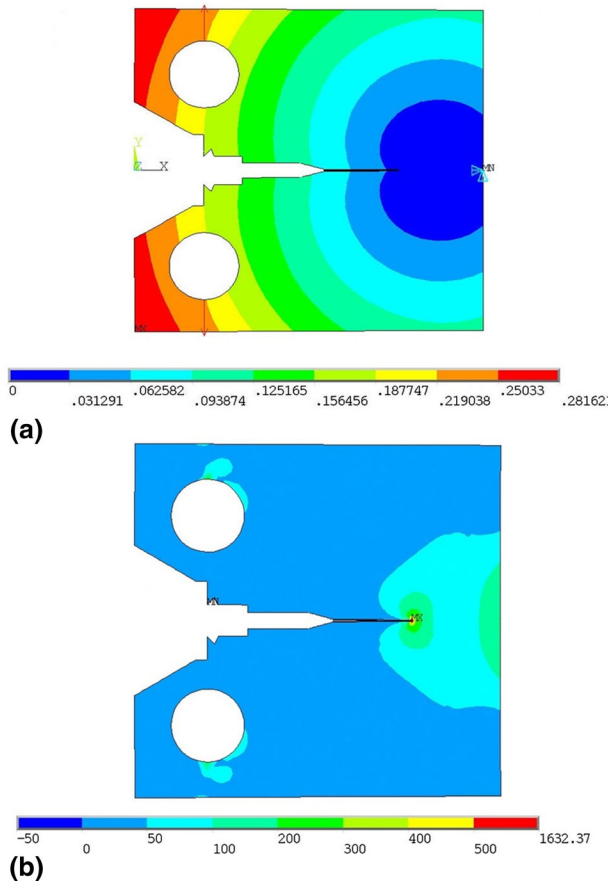
Fig. 16 (a) Displacement vector field (mm) and (b) stress contour (MPa) for load ratio 0.1 and load range 2420N

7. Conclusions

For the newly developed alloy AA 7085, three approaches to fatigue life evaluations which are fatigue crack growth model, low cycle fatigue model, and nominal stress life model are studied. The following conclusions are drawn based on the experimental and numerical study: endurance strength of the alloy calculated based on 10^6 cycles is 79.8 MPa. Investigated AA 7085 showed cyclic softening at higher strain amplitude i.e., 1.5 and 1%, while it shows mild softening for strain amplitude of 0.7%. AA 7085 is seen as following the non-Masing model. Paris and Walkar material parameters of the alloy have been calculated for the prediction of zone two of fatigue crack growth. XFEM has been utilized for the simulation of fatigue crack growth of alloy at load ratios of 0.1 and 0.3. The experimental and numerical results present a very good match. Fracture surface morphologies studied by SEM indicate that in some cases there are multiple numbers of cycles between two consecutive striation marks.

References

1. C. Li and D. Chen, Investigation on the Quench Sensitivity of 7085 Aluminum Alloy with Different Contents of Main Alloying Elements, *Metals*, 2019, **9**, p 965

2. C. Li, S. Wang, D. Zhang, S. Liu, Z. Shan and X. Zhang, Effect of Zener-Hollomon Parameter on Quench Sensitivity of 7085 Aluminum Alloy, *J. Alloy. Compd.*, 2016, **688**, p 456–462

3. Y.L. Wang, Q.L. Pan, L.L. Wei, B. Li and Y. Wang, Effect of Retrogression and Reaging Treatment on the Microstructure and Fatigue Crack Growth Behavior of 7050 Aluminum Alloy Thick Plate, *Mater. Des.*, 2014, **55**, p 857–863

4. D.J. Chakrabarti, R.R.S. J. Liu, and G.B. Venema, New Generation High Strength High Damage Tolerance 7085 Thick Alloy Product with Low Quench Sensitivity, *9th International Conference on Aluminium Alloys*, 2004, 28, pp. 6–11

5. T. Ram Prabhu, An Overview of High-Performance Aircraft Structural Al Alloy-aa7085, *Acta Metal. Sinica (Engl. Lett.)*, 2015, **28**, p 909–921

6. T. Dursun and C. Soutis, Recent Developments in Advanced Aircraft Aluminium Alloys, *Mater. Des.*, 2014, **56**, p 862–871

7. S.K. Kairy, S. Turk, N. Birbilis and A. Shekhter, The Role of Microstructure and Microchemistry on Intergranular Corrosion of Aluminium Alloy AA7085-T7452, *Corros. Sci.*, 2018, **143**, p 414–427

8. P. Dai, X. Luo, Y. Yang, Z. Kou, B. Huang, J. Zang and B. Ru, The fracture behavior of 7085–T74 Al alloy ultra-thick plate during high cycle fatigue, *Metall. Mater. Trans. A*, 2020, **51**, p 3248–3255

9. H. Luong and M.R. Hill, The Effects of Laser Peening on High-Cycle Fatigue in 7085–T7651 Aluminum Alloy, *Mater. Sci. Eng. A*, 2008, **477**, p 208–216

10. R.T. Shuey, F. Barlat, M.E. Karabin and D.J. Chakrabarti,Experimental and Analytical Investigations on Plane Strain Toughness for 7085 Aluminum Alloy, *Metall. Mater. Trans. A*, 2009, **40**, p 365–376

11. J.T. Burns and J. Boselli, Effect of Plate Thickness on the Environmental Fatigue Crack Growth Behavior of AA7085-T7451, *Int. J. Fatigue*, 2016, **83**, p 253–268

12. M.E. Karabin, F. Barlat and R.T. Shuey, Finite Element Modeling of Plane Strain Toughness for 7085 Aluminum Alloy, *Metall. Mater. Trans. A*, 2009, **40**, p 354–364

13. P. Kumar and A. Singh, Experimental and Numerical Investigations of Cyclic Plastic Deformation of Al-Mg Alloy, *J. Mater. Eng. Perform. Springer, US*, 2019, **28**, p 1428–1440

14. P. Paris and F. Erdogan, A Critical Analysis of Crack Propagation Laws, *J. Fluids Eng. Trans. ASME*, 1963, **85**, p 528–533

15. A. Papangelo, R. Guarino, N. Pugno and M. Ciavarella, On Unified Crack Propagation Laws, *Eng. Fract. Mech.*, 2019, **207**, p 269–276

16. K. Walker, The Effect of Stress Ratio During Crack Propagation and Fatigue for 2024-T3 and 7075-T6 Aluminum, *Effects of Environment and Complex Load History on Fatigue Life*, 2009, pp. 1-1–14

17 P.-M.M.H. Salimi and S. Kiad, Stochastic Fatigue Crack Growth Analysis for Space System Reliability, *ASCE-ASME J. Risk Uncert. Engrg. Sys. Part B Mech. Engrg.*, 2018, **4**, p 01–1002

18. H.O.F.R.I. Stephens, A. Fatemi and R.R. Stephens, *Metal Fatigue in Engineering*, Wiley, Hoboken, 2001

19. N.E. Dowling, *Mechanical Behavior of Materials: Engineering Methods for Deformation, Fracture, and Fatigue*, Pearson, London, 2012

20. P. Kumar, H. Pathak and A. Singh, Fatigue Crack Growth Behavior of Thermo-Mechanically Processed AA 5754: Experiment and Extended Finite Element Method Simulation, *Mech. Adv. Mater. Struct.*, 2021, **28**, p 88–101

21. A. Azarniya, A.K. Taheri and K.K. Taheri, Recent Advances in Ageing of 7xxx Series Aluminum Alloys: A Physical Metallurgy Perspective, *J. Alloy. Compd.*, 2019, **781**, p 945–983

22 T.L. Anderson, *Fracture Mechanics: Fundamentals and Applications*, CRC Press, Boca Raton, 2017

23. V. Pandey, K. Chattopadhyay, N.C. SanthiSrinivas and V. Singh, Role of Ultrasonic Shot Peening on Low Cycle Fatigue Behavior of 7075 Aluminium Alloy, *Int. J. Fatigue*, 2017, **103**, p 426–435

24. Y. Jiang and J. Zhang, Benchmark Experiments and Characteristic Cyclic Plasticity Deformation, *Int. J. Plast*, 2008, **24**, p 1481–1515

25. S.K. Paul, S. Sivaprasad, S. Dhar and S. Tarafder, Cyclic Plastic Deformation and Damage in 304LN Stainless Steel, *Mater. Sci. Eng. A*, 2011, **528**, p 4873–4882

26. A.K. Wong and G.C. Kirby, A Hybrid Numerical/Experimental Technique for Determining the Heat Dissipated During Low Cycle Fatigue, *Eng. Fract. Mech.*, 1990, **37**, p 493–504

27. S.K. Paul, Correlation Between Endurance Limit and Cyclic Yield Stress Determined from Low Cycle Fatigue Test, *Materialia*, 2020, **11**, p 100695

28. T. Zhao, J. Zhang and Y. Jiang, A Study of Fatigue Crack Growth of 7075–T651 Aluminum Alloy, *Int. J. Fatigue*, 2008, **30**, p 1169–1180

29. J.C. Newman and K.F. Walker, Fatigue-Crack Growth in Two Aluminum Alloys and Crack-Closure Analyses Under Constant-Amplitude and Spectrum Loading, *Theoret. Appl. Fract. Mech.*, 2019, **100**, p 307–318

30. S. Chowdhury, M. Deeb and V. Zabel, Effects of Parameter Estimation Techniques and Uncertainty on the Selection of Fatigue Crack Growth Model, *Structures*, 2019, **19**, p 128–142

31. A. Shyam and E. Lara-Curzio, A Model for the Formation of Fatigue Striations and its Relationship with Small Fatigue Crack Growth in an Aluminum Alloy, *Int. J. Fatigue*, 2010, **32**, p 1843–1852